materials

MDPI

Article

Novel Porous Phosphorus–Calcium–Magnesium Coatings on Titanium with Copper or Zinc Obtained by DC Plasma Electrolytic Oxidation: Fabrication and Characterization

Krzysztof Rokosz [1,*], Tadeusz Hryniewicz [1], Sofia Gaiaschi [2], Patrick Chapon [2], Steinar Raaen [3], Dalibor Matýsek [4], Łukasz Dudek [1] and Kornel Pietrzak [1]

1 Division of BioEngineering and Surface Electrochemistry, Department of Engineering and Informatics Systems, Koszalin University of Technology, Racławicka 15-17, PL 75-620 Koszalin, Poland; Tadeusz.Hryniewicz@tu.koszalin.pl (T.H.); lukasz.dudek@tu.koszalin.pl (Ł.D.); kornel.pietrzak@s.tu.koszalin.pl (K.P.)

2 HORIBA FRANCE S.A.S., Avenue de la Vauve, Passage Jobin Yvon, 91120 Palaiseau, France; sofia.gaiaschi@horiba.com (S.G.); patrick.chapon@horiba.com (P.C.)

3 Department of Physics, Norwegian University of Science and Technology (NTNU), Realfagbygget E3-124 Høgskoleringen 5, 7491 NO Trondheim, Norway; steinar.raaen@ntnu.no

4 Institute of Geological Engineering, Faculty of Mining and Geology, VŠB—Technical University of Ostrava, 708 33 Ostrava, Czech Republic; dalibor.matysek@vsb.cz

* Correspondence: rokosz@tu.koszalin.pl; Tel.: +48-501-989-332

Received: 2 August 2018; Accepted: 7 September 2018; Published: 11 September 2018

Abstract: In this paper, the characteristics of new porous coatings fabricated at three voltages in electrolytes based on H_3PO_4 with calcium nitrate tetrahydrate, magnesium nitrate hexahydrate, and copper(II) nitrate trihydrate are presented. The SEM, energy dispersive spectroscopy (EDS), glow discharge optical emission spectroscopy (GDOES), X-ray photoelectron spectroscopy (XPS), and XRD techniques for coating identification were used. It was found that the higher the plasma electrolytic oxidation (PEO) (micro arc oxidation (MAO)) voltage, the thicker the porous coating with higher amounts of built-in elements coming from the electrolyte and more amorphous phase with signals from crystalline $Ca(H_2PO_4)_2 \cdot H_2O$ and/or $Ti(HPO_4)_2 \cdot H_2O$. Additionally, the external parts of the obtained porous coatings formed on titanium consisted mainly of Ti^{4+}, Ca^{2+}, Mg^{2+} and PO_4^{3-}, HPO_4^{2-}, $H_2PO_4^{-}$, $P_2O_7^{4-}$ as well as Zn^{2+} or copper Cu^{+}/Cu^{2+}. The surface should be characterized by high biocompatibility, due to the presence of structures based on calcium and phosphates, and have bactericidal properties, due to the presence of zinc and copper ions. Furthermore, the addition of magnesium ions should accelerate the healing of postoperative wounds, which could lead to faster patient recovery.

Keywords: micro arc oxidation; plasma electrolytic oxidation; DC PEO; DC MAO; titanium; calcium nitrate tetrahydrate; magnesium nitrate hexahydrate; copper(II) nitrate trihydrate; 85% phosphoric acid

1. Introduction

The phenomenon of luminescence occurring on the surface of metals during the galvanic process was first observed by Sluginov in 1880 [1], and the information was published for the first time by Braun in 1898 [2]. In 1929, Dufford showed that during the electrolysis of metals such as aluminum, zinc, silver, tantalum, tungsten, magnesium, cerium, antimony, and mercury in selected electrolytes, the phenomenon of luminescence was observed [3]. In addition, he noticed that this phenomenon

was not observed with lead, iron, copper, nickel, molybdenum, tin, and platinum. Such luminescence phenomenon was developed, *inter alia*, by McNeill, Gruss, Yerokhin, and Nie [4,5]. In addition, Yerokhin at al. proposed a definition of that process, that it is "an electrolytic treatment of anodically polarized metal surfaces carried out above the dielectric breakdown voltage of the growing oxide film", as well as an explanation of the formation of porous coatings [5,6]. According to this theory, during small voltage polarization, the passive layer is forming, which may be dissolved with the voltage increase. Further increases of voltage result in film repassivation and growth of a new porous oxide film. In the next step of voltage increase, the electric field strength in the oxide film reaches a critical value, after which the film is broken through due to impact or tunneling ionization (here, luminescent sparks are observed). A further increase of voltage results in the following: thermal ionization, larger arc discharges, film fusing and alloying with electrolyte elements, microdischarges penetrating through to the substrate, powerful arcs, destructive effects, and thermal cracking of the coating. It should be also pointed out that on the same plasma electrolytic oxidation (PEO) treated surface, more than one of the described processes may occur concurrently [5]. Over the years, the phenomenon of galvanic luminescence occurring during the anodic polarization of selected metals and electrolytes has been defined as microplasma oxidation, anode spark electrolysis, plasma electrolytic anode treatment, plasma electrolytic oxidation, or micro arc oxidation [7]. Systematic studies proposed coating growth [8–10] and discharging [11–14] behaviors as well as electrolyte influence on the ignition of plasma electrolytic oxidation processes [15]. Meanwhile, Curran and Clyne described the thermophysical properties of plasma electrolytic oxidation [16] and the porosity of PEO coatings [17]. Other authors studied oxygen evolution during PEO [18] and the effects of electrical parameters on that process [19] as well as phase formation in ceramic PEO coatings [20,21] and their corrosion resistance [22]. The PEO process has been performed by researchers under different conditions, i.e., DC [23,24], AC [25,26], and pulse [27,28] currents, which result in different surface morphology [29,30] and chemical composition [31,32] as well as mechanical [33,34] and electrochemical properties [35,36]. For the most frequently treated materials by PEO processes, aluminum [37–40] and its alloys [40–44], magnesium [45] and its alloys [46–54], titanium [55–60] and its alloys [61–67], zirconium [68–77] and its alloys [78,79], tantalum [80–83], niobium [84–88], and hafnium [89] should be included. In the present paper, PEO coatings obtained on titanium in novel electrolytes, which have never been used or described in the literature until now, are presented (Table 1). These electrolytes are based on orthophosphoric acid and three different nitrates.

Table 1. Electrolytes and conditions of the plasma electrolytic oxidation (PEO) process.

Electrolytes	Voltage Current Density	Ref.
H_2O, $NaAlO_2$, $Na_3PO_4{\cdot}12H_2O$, KOH, NaCl	100–900 mA·cm^{-2} (f = 50 Hz)	[7]
H_2O, $Na_3PO_4{\cdot}12H_2O$, KOH, Na_2SO_4, $(HOCH_2)_3CNH_2$, $(NH_4)_2HPO_4$, $C_2H_7NO_2$	70 mA·cm^{-2} (f = 50 Hz)	[23]
H_3PO_4, $Ca(NO_3)_2{\cdot}4H_2O$, $Mg(NO_3)_2{\cdot}6H_2O$, $Cu(NO_3)_2{\cdot}3H_2O$, $Zn(NO_3)_2{\cdot}6H_2O$	500, 575, 650 V	[24]
H_3PO_4, $Cu(NO_3)_2{\cdot}3H_2O$	450 V	[32]
H_2O, Na_2SiO_3, $(NaPO_3)_6$, $NaAlO_2$ microparticle	80 mA·cm^{-2} (f = 300 Hz)	[33]
H_3PO_4, $Mg(NO_3)_2{\cdot}6H_2O$, $Zn(NO_3)_2{\cdot}6H_2O$	500–650 V	[35]
H_2O, Na_3PO_4, $FeSO_4$	350 V (f = 100 Hz)	[55]
H_2O, $NaAlO_2$, KOH	400 V (f = 2000 Hz)	[56]
H_2O, $(CH_3COO)_2Ca{\cdot}H_2O$, $NaH_2PO_4{\cdot}2H_2O$	300, 390 V (f = 900 Hz)	[58]
H_2O, $Ca(CH_3COO)_2$,$Sr(CH_3COO)_2$	400, 450 V (f = 100 Hz)	[59]
H_3PO_4, $Ca(NO_3)_2{\cdot}4H_2O$	500, 575, 650 V	[60]
H_2O, Na_3PO_4, $Co(CH_3COO)_2$	350 V (f = 100 Hz)	[61]
H_2O, $Na_3PO_4{\cdot}12H_2O$, $Na_2B_4O_7{\cdot}10H_2O$, $Na_3WO_4{\cdot}2H_2O$	50 mA·cm^{-2}	[62]
H_2O, Na_2SiO_3, Na_2CO_3, NaOH	12 mA·cm^{-2} (f = 100 Hz)	[63]
H_2O, $C_6H_{18}O_{24}P_6$, KOH, EDTA-Na_2, $Ca(CH_3COO)_2$	20, 50, 80 V	[64]
H_2O, $NaAlO_2$, Na_2SiO_3, $(NaPO_3)_6$	550 V	[65]
H_2O, Na_2HPO_4, $C_4H_6O_4Ca{\cdot}H_2O$	+400 V/−80 V (f = 250 Hz)	[66]
H_2O, $C_3H_9O_6P$, $C_4H_6O_4Ca{\cdot}H_2O$	+400 V/−80 V (f = 250 Hz)	[66]
H_2O, Na_2HPO_4, $C_3H_7CaO_6P{\cdot}H_2O$	+400 V/−80 V (f = 250 Hz)	[66]
H_2O, $(CH_3COO)_2Ca{\cdot}H_2O$, $NaH_2PO_4{\cdot}H_2O$	350–500 V (f = 1000 Hz)	[67]
H_2O, $Ca(CH_3COO)_2{\cdot}H_2O$	300 V (f = 1000 Hz)	[90]
H_2O, $(CH_1COO)_2Ca$, $C_3H_7Na_2O_6P$	250–400 V (f = 100 Hz)	[91]
H_2O, $(CH_3COO)_2Ca{\cdot}H_2O$, $C_3H_7Na_2O_6P{\cdot}5H_2O$	450 V (f = 100 Hz)	[92]

Table 1. *Cont.*

Electrolytes	Voltage Current Density	Ref.
H_2O, $(CH_3COO)_2Ca{\cdot}H_2O$, $C_3H_7Na_2O_6P{\cdot}5H_2O$	250–500 V (f = 1000 Hz)	[93,94]
H_2O, $Ca(CH3COO)_2{\cdot}H_2O$, $CaC_3H_7O_6P$	190–600 V (f = 660 Hz)	[95,96]
H_2O, $(CH_3COO)_2Ca{\cdot}H_2O$, $C_3H_7Na_2O_6P{\cdot}5H_2O$	200–500 V (f = 900 Hz)	[97]
H_2O, $Na4P_2O_7{\cdot}10H_2O$ and KOH, $NaAlO_2$	0–300 V	[98]
$Na_2B_4O_7{\cdot}10H_2O$, $(CH_3COO)_2Mn{\cdot}4H_2O$	450–500 V	[99]
H_2O, $(CH_3COO)_2Ca{\cdot}H_2O$	230 V	[100]
H_2O, $(CH_3COO)_2Ca{\cdot}H_2O$, $NaH_2PO_4{\cdot}2H_2O$	260–420 V	[101]
H_2O, $CaHPO_4$, $Ca(H_2PO_4)_2$, $Na_6P_6O_{18}$, $Ca(CH_3COO)_2$	20, 100 mA·cm^{-2}	[102]
H_2O, KOH	290 V (f = 100–200 Hz)	[103]
H_2O, KOH	350 V (f = 1000 Hz)	[104]
H_2O, $(NaPO_3)_6$, NaF, $NaAlO_2$	150–200 V	[105]
H_2O, $K_2Al_2O_4$, Na_3PO_4, NaOH	400 V	[106]
H_2O, $CaCl_2$ and KH_2PO_4	320–340 V	[107]
H_2O, H_2SO_4 and $Ti_2(SO_4)_3$	1100 V	[108]
H_2O, Na_2(EDTA), CaO, $Ca(H_2PO_4)_2$, $Na_2SiO_3{\cdot}H_2O$	350 V (f = 200 Hz)	[109]
H_2O, Na_2SiO_3, NaOH	280 V	[110]
H_2O, CaO, $Na_6P_6O_{18}$, $Na_2H_2EDTA{\cdot}5.5H_2O$, KOH	AC 0.5–2 mA·cm^{-2}	[111]
$_2O$, $(NaPO_3)_6$, NaF, $NaAlO_2$	60 mA·cm^{-2} (f = 100, 600 Hz)	[112]
H_2O, Na_3PO_4, $FeSO_4$, $Co(CH_3COO)_2$, $Ni(CH_3COO)_2$, K_2ZrF_6	350 V (f = 100 Hz)	[113]
H_2O, $Ca(CH_3COO)_2{\cdot}H_2O$, $C_3H_7Na_2O_6P$	150 V	[114]
H_2O, $Na_2SiO_3{\cdot}9H_2O$, $Na_3PO_4{\cdot}12H_2O$, $Na_2SiO_3{\cdot}9H_2O$, $Na_3PO_4{\cdot}12H_2O$	80 mA·cm^{-2} (f = 150 Hz)	[115]
H_2O, $Na_3PO_4{\cdot}12H_2O$, α-Al_2O_3 nanoparticles	20 mA·cm^{-2}	[116]

It should also be pointed out that in hydroxyapatite-like structures it is possible to substitute the Ca^{2+} ions for Ca^{2+}, Mg^{2+}, Cu^{2+}, and Zn^{2+}, as well as OH^- for Cu^+, which will be used in the fabrication of novel PEO coatings. The porous calcium–phosphate coatings obtained on titanium [117–119] and enriched with biocompatible magnesium, which causes faster wound healing [120–125], as well as antibacterial zinc [126–132] and copper [133–136], may be used as biomaterial, which will be fully accepted by the tissue environment.

However, without results *inter alia* presented in those papers, it is not possible to predict the real possibility of that substitution during plasma treatment in electrolyte in which the ions are present, as well as the thickness and porosity of the PEO coatings. Therefore, in the present paper, the results of x-ray photoelectron spectroscopy (XPS) (10 top nanometers) will be helpful in explaining the oxidation states of those chemical elements as well as chemical composition for all volumes, thicknesses, and pore shapes of obtained coatings by energy dispersive spectroscopy (EDS), XRD, glow discharge optical emission spectroscopy (GDOES), and SEM.

2. Materials and Methods

Porous coatings obtained on titanium samples (10 × 10 × 2 mm) by PEO treatment in electrolyte (constant volume of 500 mL for each experiment) containing phosphoric acid (85% *w*/*w*) with the addition of calcium nitrate tetrahydrate $Ca(NO_3)_2{\cdot}4H_2O$, magnesium nitrate hexahydrate $Mg(NO_3)_2{\cdot}6H_2O$, and copper(II) nitrate trihydrate $Cu(NO_3)_2{\cdot}3H_2O$ in weight ratios of 1:1:1 (Table 2) at 3 voltages, 500 V (PEO time: 3 min), 575 V (PEO times: 1, 3, 5 min), and 600 V (PEO time: 3 min), using a PWR 1600H power supply (KIKUSUI Electronics Corp., Yokohama, Kanagawa, Japan) were fabricated. For their characterization, the complementary measurement methods SEM, EDS, GDOES, XPS, and XRD [137–141] were used. Descriptions of the setups are presented in Table 3 and are detailed in reference [24].

Table 2. Experimental plan and code sample names.

Sample Name	Voltage	Electrolyte Type	Electrolyte Composition	
			Salts	Salt Concentrations (g/L)
Ti_CaMgZn_500V	500 V	Electrolyte 1	$Ca(NO_3)_2{\cdot}4H_2O$ and $Mg(NO_3)_2{\cdot}6H_2O$ & $Zn(NO_3)_2{\cdot}6H_2O$	166.7 + 166.7 + 166.7
Ti_CaMgZn_575V	575 V			
Ti_CaMgZn_650V	650 V			
Ti_CaMgCu_500V	500 V	Electrolyte 2	$Ca(NO_3)_2{\cdot}4H_2O$ and $Mg(NO_3)_2{\cdot}6H_2O$ & $Cu(NO_3)_2{\cdot}3H_2O$	166.7 + 166.7 + 166.7
Ti_CaMgCu_575V	575 V			
Ti_CaMgCu_650V	650 V			

Table 3. Setups of SEM, energy dispersive spectroscopy (EDS), x-ray photoelectron spectroscopy (XPS), glow discharge optical emission spectroscopy (GDEOS), and XRD equipment.

Technique	Equipment	Manufacturer
SEM	Quanta 650 FEI	Field Electron and Iron Company, Hillsboro, OR, USA
EDS	Noran System Six	EDS, Silicon Drift Detectors: Keith Thompson, Thermo Fisher Scientific, Madison, WI, USA
XPS	SCIENCE SES 2002	Scienta AB, Scienta Omicron, Uppsala, Sweden
GDOES	GD Profiler 2	HORIBA Scientific, Palaiseau, France
XRD	Bruker-AXS D8 Advance	Bruker Corporation, Billerica, MA, USA

3. Results

Figure 1 shows the surface morphologies of coating surfaces formed on titanium at 500 V, 575 V, and 650 V in two different electrolytes based on phosphoric acid. Two solutions were used: Electrolyte 1, containing H_3PO_4 with the addition of calcium nitrate tetrahydrate $Ca(NO_3)_2 \cdot 4H_2O$, magnesium nitrate hexahydrate $Mg(NO_3)_2 \cdot 6H_2O$, and zinc nitrate hexahydrate $Zn(NO_3)_2 \cdot 6H_2O$; and Electrolyte 2, with additions of calcium nitrate tetrahydrate $Ca(NO_3)_2 \cdot 4H_2O$, magnesium nitrate hexahydrate $Mg(NO_3)_2 \cdot 6H_2O$, and copper(II) nitrate trihydrate $Cu(NO_3)_2 \cdot 3H_2O$. It should be pointed out that all the obtained coatings were porous and had a well-developed surface.

In Figure 2 and Table 4, the EDS semiquantitative results for samples obtained in Electrolyte 1 are presented as Ca/P, Mg/P, Zn/P, and M/P ratios. The Ca/P ratios were equal to 0.051 ± 0.003 natural units (n.u.), 0.063 ± 0.003 n.u., and 0.069 ± 0.003 n.u. for 500, 575, and 650 V, respectively. The Mg/P ratios were equal to 0.051 ± 0.004 n.u. (500 V), 0.058 ± 0.003 n.u. (575 V), and 0.060 ± 0.006 n.u. (650 V). The Zn/P ratios for 500, 575, and 650 V were equal to 0.052 ± 0.004 n.u., 0.065 ± 0.005 n.u., and 0.071 ± 0.010 n.u., respectively. The M/P ratios were equal to 0.153 ± 0.008, 0.187 ± 0.006, and 0.200 ± 0.020 for 500, 575, and 650 V, respectively.

Figure 3 and Table 5 present the EDS semiquantitative results for samples obtained in Electrolyte 2 as Ca/P, Mg/P, Cu/P, and M/P. The Ca/P ratios were equal to 0.062 ± 0.003 n.u., 0.068 ± 0.004 n.u., and 0.071 ± 0.003 n.u. for 500, 575, and 650 V, respectively. The Mg/P ratios were equal to 0.058 ± 0.002 n.u., 0.059 ± 0.003 n.u., and 0.064 ± 0.003 n.u. for 500, 575, and 650 V, respectively. The Cu/P ratios for samples obtained at 500, 575, and 650 V were equal to 0.039 ± 0.003 n.u., 0.048 ± 0.002 n.u., and 0.062 ± 0.005 n.u., respectively. The M/P ratios for samples obtained at 500, 575, and 650 V were equal to 0.158 ± 0.006 n.u., 0.175 ± 0.006 n.u., and 0.197 ± 0.004 n.u., respectively.

Table 4. Statistical description of EDS of coatings formed in Electrolyte 1. n.u., no units.

Ratios	Voltage	$\bar{x}$	σ	Q_1	Q_2	Q_3
Ca/P n.u.	500 V	0.051	0.003	0.050	0.052	0.052
	575 V	0.063	0.003	0.062	0.064	0.065
	650 V	0.069	0.003	0.068	0.071	0.071
Mg/P n.u.	500 V	0.051	0.004	0.049	0.051	0.053
	575 V	0.058	0.003	0.057	0.060	0.060
	650 V	0.060	0.006	0.057	0.063	0.063
Zn/P n.u.	500 V	0.052	0.004	0.050	0.053	0.054
	575 V	0.065	0.005	0.063	0.068	0.068
	650 V	0.071	0.010	0.065	0.075	0.075
M/P n.u.	500 V	0.153	0.008	0.149	0.151	0.157
	575 V	0.187	0.006	0.184	0.188	0.190
	650 V	0.200	0.015	0.192	0.195	0.206

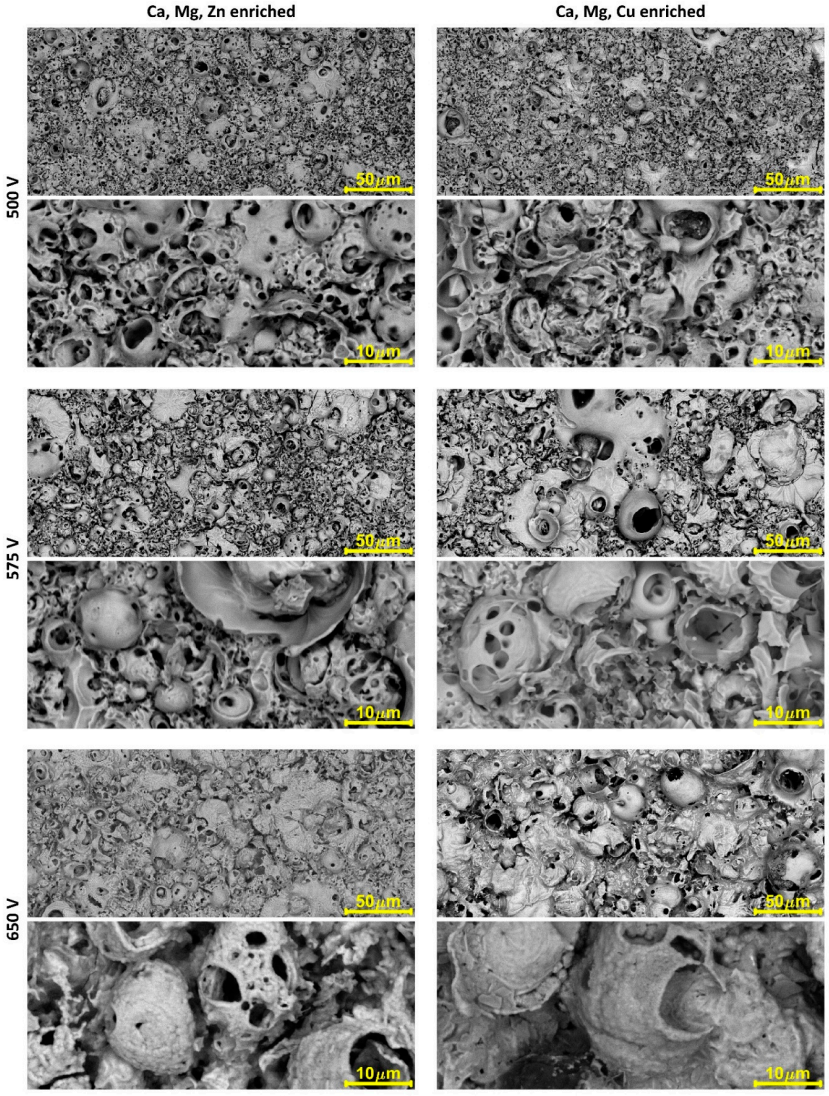

Figure 1. Surface morphologies of surfaces after PEO processing.

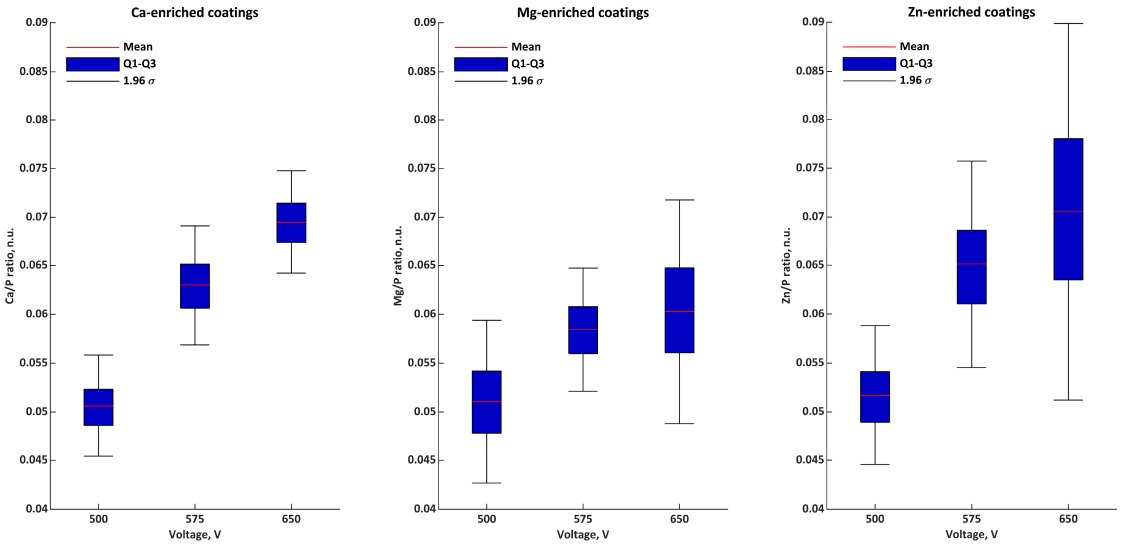

Figure 2. Atomic ratios (EDS) of coatings formed in Electrolyte 1.

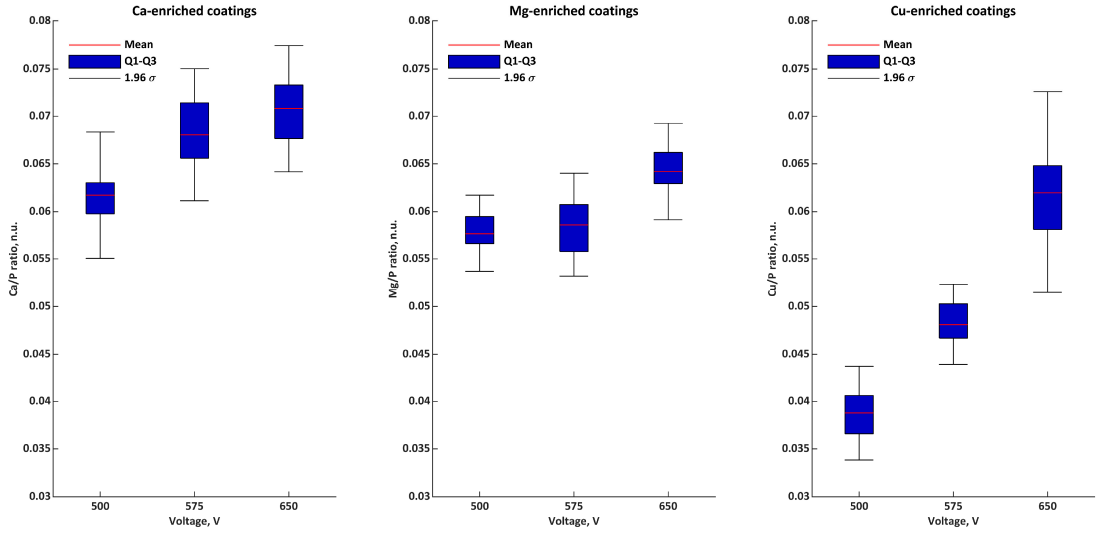

Figure 3. Atomic ratios (EDS) of coatings formed in Electrolyte 2.

Table 5. Statistical description of EDS of coatings formed in Electrolyte 2. n.u., no units.

Ratios	Voltage	$\bar{x}$	σ	Q_1	Q_2	Q_3
Ca/P n.u.	500 V	0.062	0.003	0.060	0.061	0.062
	575 V	0.068	0.004	0.066	0.068	0.071
	650 V	0.071	0.003	0.068	0.072	0.073
Mg/P n.u.	500 V	0.058	0.002	0.057	0.057	0.059
	575 V	0.059	0.003	0.056	0.060	0.061
	650 V	0.064	0.003	0.064	0.064	0.066
Cu/P n.u.	500 V	0.039	0.003	0.037	0.040	0.040
	575 V	0.048	0.002	0.047	0.048	0.050
	650 V	0.062	0.005	0.059	0.061	0.063
M/P n.u.	500 V	0.158	0.006	0.156	0.156	0.159
	575 V	0.175	0.006	0.172	0.176	0.177
	650 V	0.197	0.004	0.195	0.196	0.197

The diffraction data of PEO coatings formed in Electrolytes 1 and 2 at three voltages are presented in Figure 4. For both electrolytes, similar phenomena were observed, i.e., for samples oxidized at 500 and 575 V, only signal from titanium as metal matrix was detected, while for 650 V other crystalline phases, such as $Ca(H_2PO_4)_2 \cdot H_2O$ and $Ti(HPO_4)_2 \cdot H_2O$ for samples obtained in Electrolyte 1 and $Ca(H_2PO_4)_2 \cdot H_2O$ for samples obtained in Electrolyte 2, were recorded. It was also found that voltage growth in PEO coatings caused amorphous phase accretion as well.

GDOES data of PEO coatings formed in Electrolyte 1 at 500, 575, and 650 V are presented in Figure 5. The top and porous sublayers, which are enriched in Zn, P, and O and depleted in Ca, Mg, and Ti, have thicknesses of about 200, 300, and 500 s of sputtering time for 500, 575, and 650 V, respectively, while the thickness of the second (semiporous) one, which was enriched in calcium, magnesium, zinc, phosphorus, and oxygen and depleted in titanium, was in the range of 700 s (500 V) up to 2000 s (650 V) of sputtering time. On the other hand, the thicknesses of the third (transition) sublayers, in which a decrease of all signals, except titanium, was observed, increased from 800 s (500 V) up to 2000 s (650 V) of sputtering time. In Figure 6, the GDOES results of PEO coatings formed in Electrolyte 2 at the same three voltages are presented.

The top and porous sublayers, which are enriched in P and O and depleted in Ca, Mg, Cu, and Ti, have thicknesses related to sputtering times equal to about 100, 300, and 600 s for 500, 575, and 650 V, respectively, while the thickness of the second (semiporous) layer, which is enriched in Ca, Mg, Cu, P, and O and depleted in Ti, is in the range of 600 s (500 V) up to 1900 s (650 V) of sputtering time. Here, the thicknesses of the transition sublayers are in the range from 600 s (500 V) up to 1500 s (650 V) of sputtering time. The part of C, N, and O signals may originate in the first top sublayers from

contamination (from air and cleaning compounds). In addition, the H signals maxima, which are always placed in third-transition sublayers, is the end of the coating porosity. It should also be noted that the accretion of voltage caused an increase in coating thickness. In Figures 7 and 8, the XPS spectra of PEO coatings formed in Electrolytes 1 and 2 are presented. Based on the obtained results, it can be concluded that the top external 10 nm layers of the PEO coating consist mainly of phosphorus, oxygen, nitrogen, titanium, calcium, magnesium, and zinc (Electrolyte 1) or copper (Electrolyte 2). The bindings of C with O and N with O can be interpreted as contaminants (cleaning process and adsorbed air). The phosphorus (P 2p) and oxygen (O 1s) spectra were in the range of 133.6–134 eV and 531.3–531.5 eV, respectively, which can be interpreted as the groups PO_4^{3-}, HPO_4^{2-}, $H_2PO_4^{-}$, and $P_2O_7^{4-}$. The Cu 2p spectra maxima (331.1–932.9 eV and 934.5–935.8 eV) and Auger Cu LMM (566–567.2 eV) suggest the presence of Cu^{+} and Cu^{2+}, while Ca^{2+} is proved by the binding energy (BE) in the range of 347.4−347.7 eV. The BE of Zn 2p (1021.9–1022.4 eV) and Zn LMM (497.9–501.5 eV) proves the existence of Zn^{2+}, while BE in the range of 89.1–92.8 eV (Mg 2s) and 306.2–306.9 eV (Mg KLL) indicates the existence of Mg^{2+}. The BE of titanium Ti $2p_{3/}$is in the range of 459.9−460.2 eV, which means that titanium is on the fourth oxidation state (Ti^{4+}). Based on the quantitative XPS of the top 10 nm of PEO coatings obtained in Electrolytes 1 and 2 at three voltages, two ratios, Ca:Mg:Zn and Ca:Mg:Zn, were found. The Ca:Mg:Zn ratios are equal to 8:32:1 n.u. (500 V), 8:28:1 n.u. (575 V), and 14:45:1 n.u. (650 V), while the Ca:Mg:Zn ratios are equal to 5:5:1 n.u. (500 V), 4:7:1 n.u. (575 V), and 6:5:1 n.u. (650 V). (Ca + Mg + Zn)/P and (Ca + Mg + Cu)/P have their maxima equal to 0.48 n.u. and 0.21 n.u., respectively, at 575 V. The same trend was observed for single Me/P ratios, where M ∈ {Ca, Mg, Zn, Cu}, i.e., the maxima were recorded for PEO coatings obtained at 575 V.

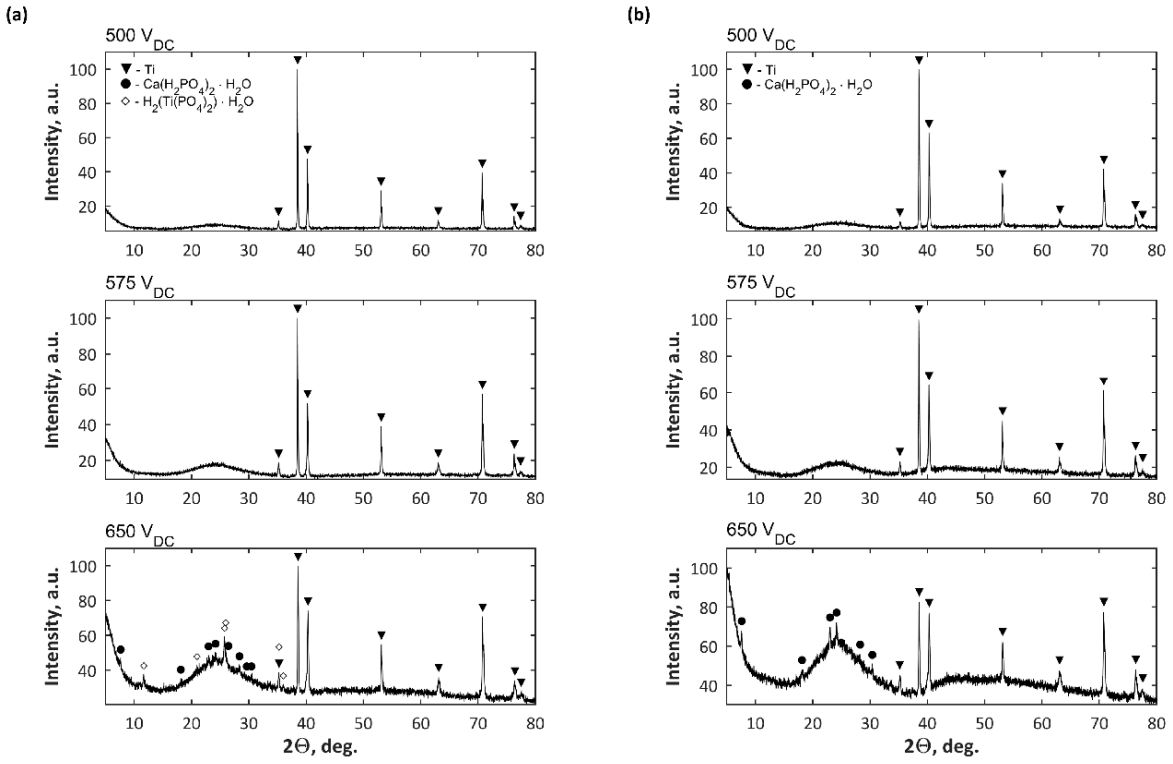

Figure 4. Diffractogram XRD results of PEO coatings obtained in (**a**) Electrolyte 1 and (**b**) Electrolyte 2.

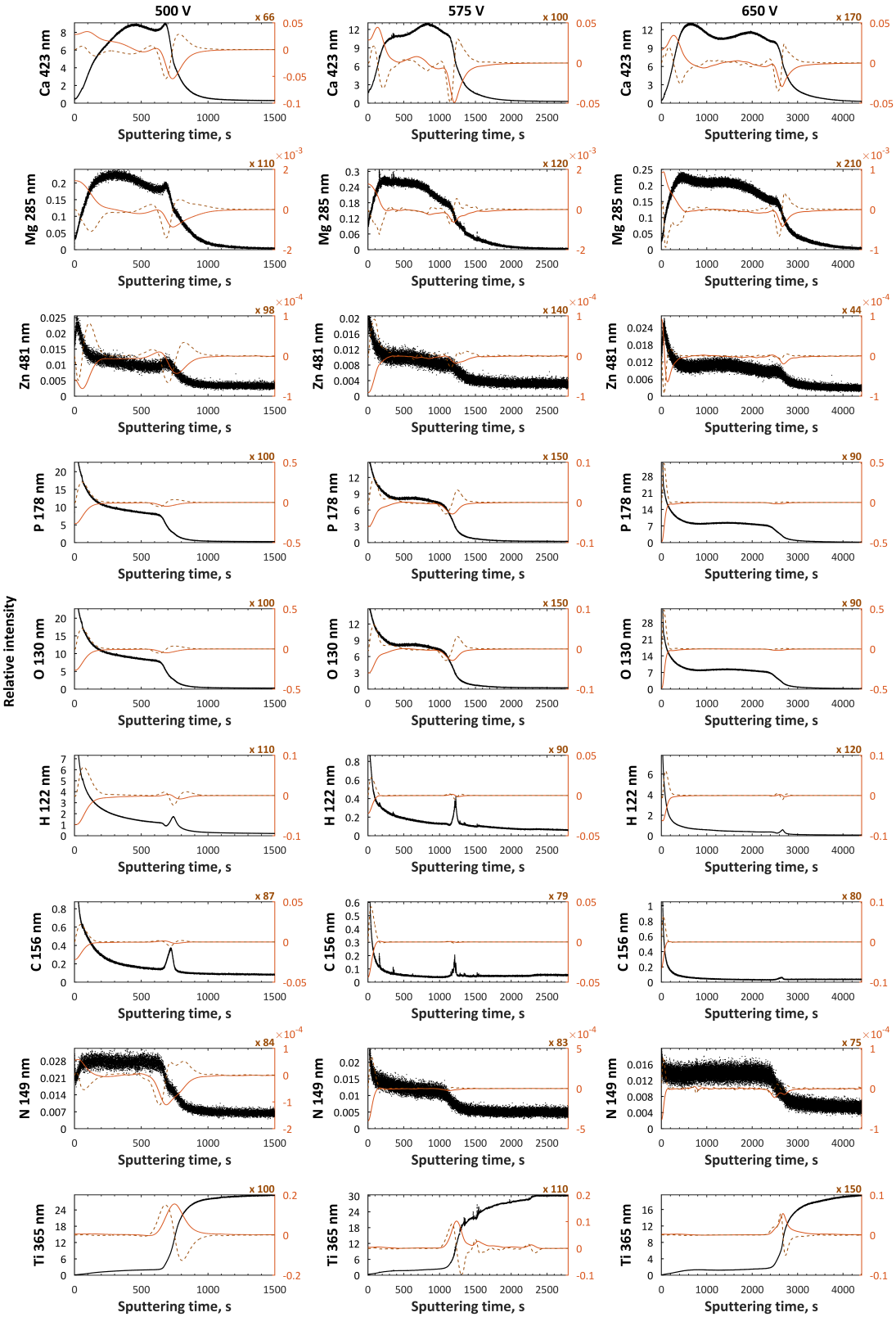

Figure 5. GDEOS signals (black), first derivatives (red continuous line), and second derivatives (brown dashed line) for samples formed in Electrolyte 1.

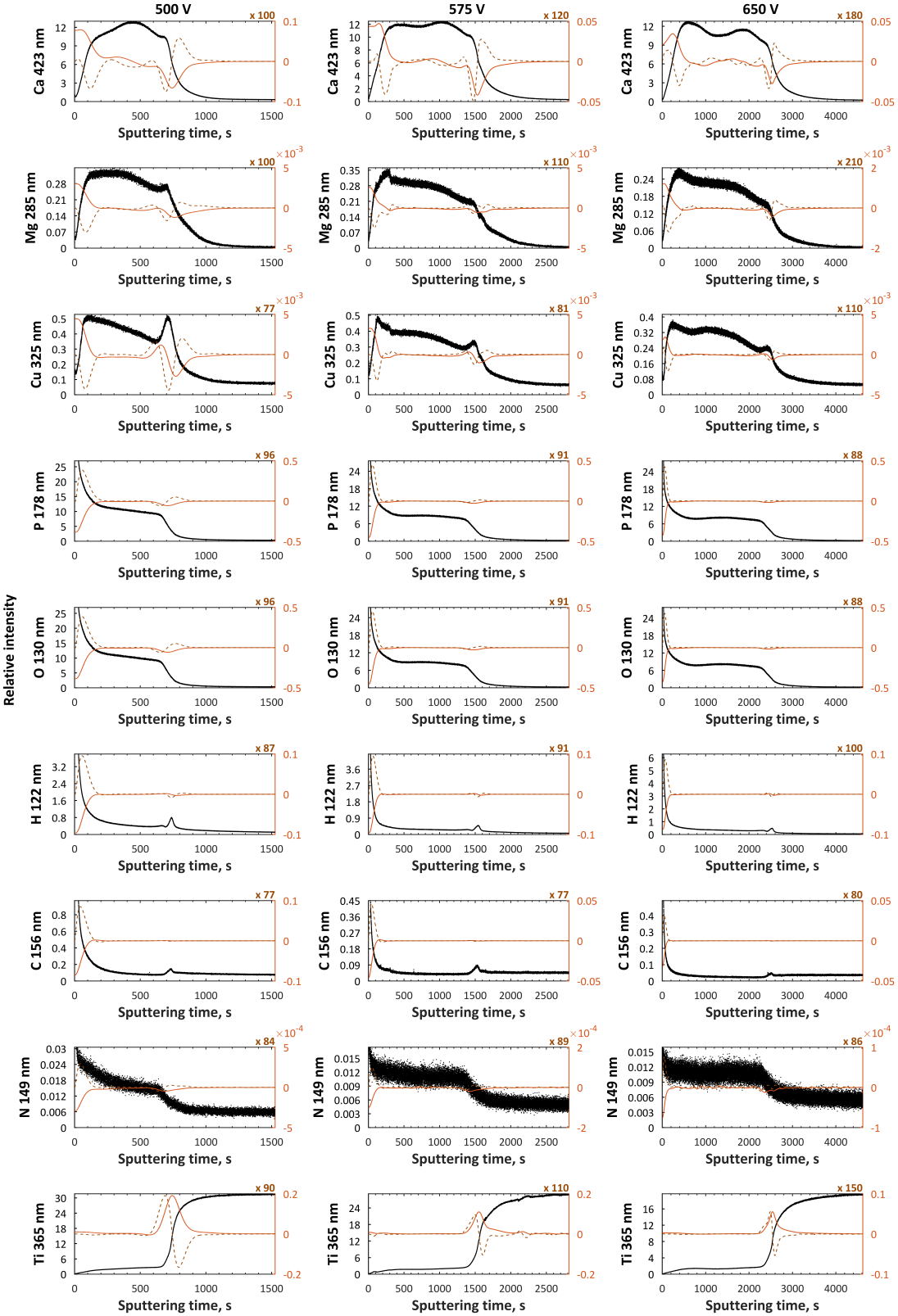

Figure 6. GDEOS signals (black), first derivatives (red continuous line), and second derivatives (brown dashed line) for samples formed in Electrolyte 2.

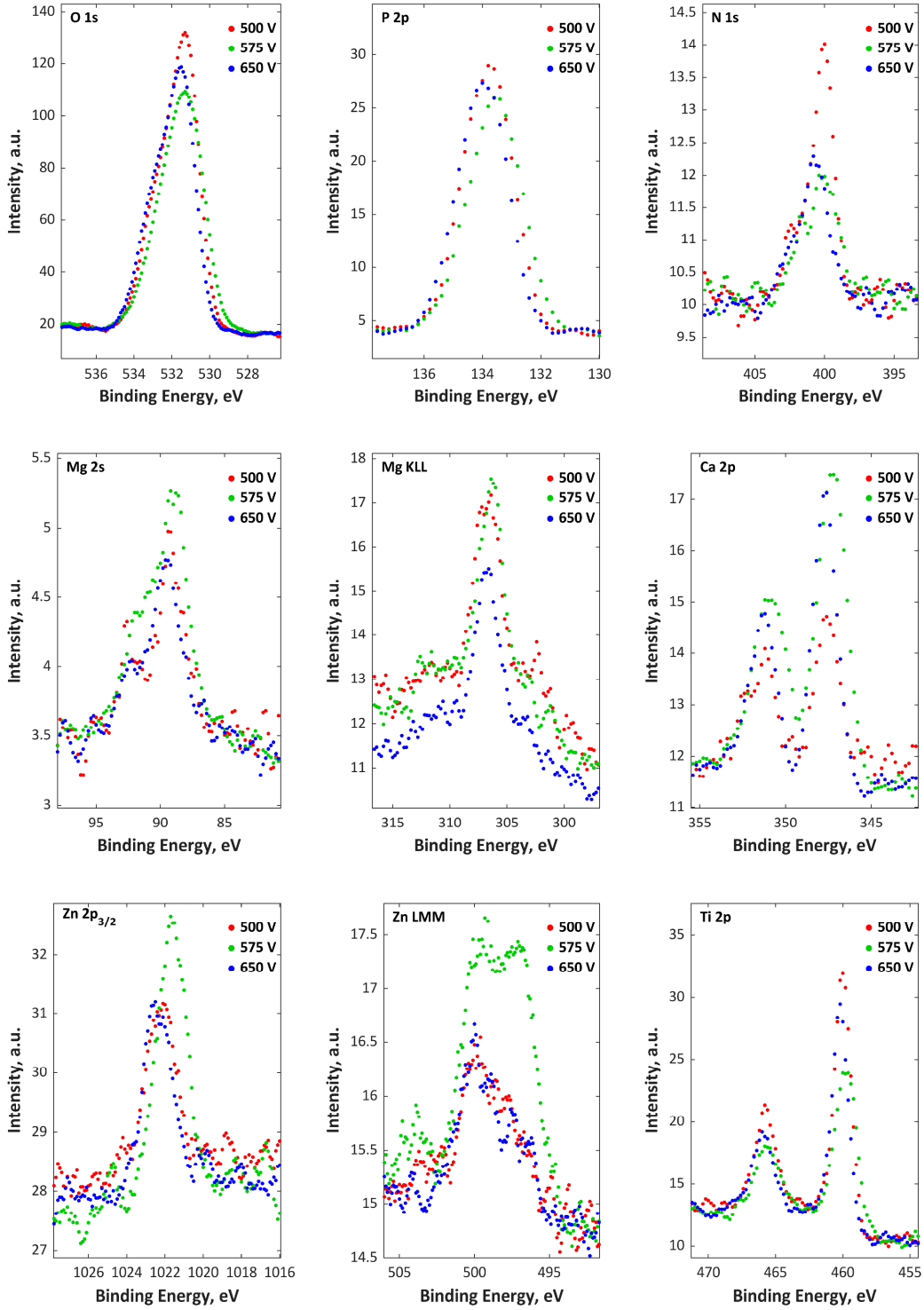

Figure 7. XPS spectra for titanium samples after PEO treatment in Electrolyte 1.

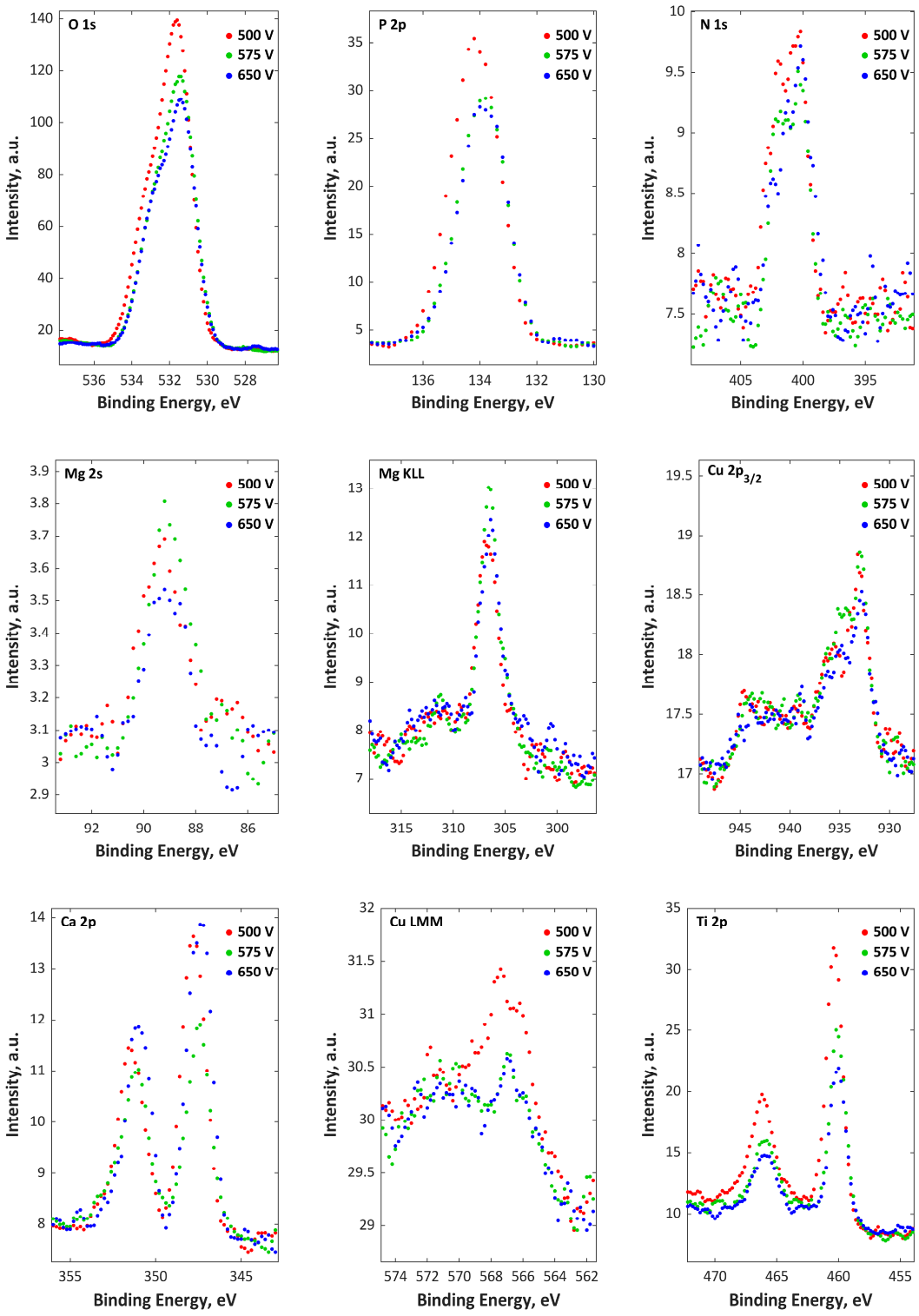

Figure 8. XPS spectra for titanium samples after PEO treatment in Electrolyte 2.

4. Discussion

In this paper, the characteristics of new porous coatings fabricated at 500, 575, and 650 V in electrolytes based on H_3PO_4 and $Mg(NO_3)_2 \cdot 6H_2O$, $Ca(NO_3)_2 \cdot 4H_2O$ with $Cu(NO_3)_2 \cdot 3H_2O$, and $Zn(NO_3)_2 \cdot 6H_2O$ were presented. Information on the chemical composition of the PEO coatings was obtained by use of the XPS method (for the first 10 nm) and EDS and XRD (for the whole volume of the coatings). Based on EDS results, which were recorded for the whole volume of the coatings, it was found that increased PEO voltage results in an increase of the average metal-to-phosphorus ratios (Ca/P, Mg/P, Zn/P, and Cu/P), while XPS analysis of 10 nm showed that the maxima of those ratios are achieved for the values of the central voltage (575 V), which indicates that the coatings are layered, as proven by GDOES elemental profiles. All the PEO coatings can be divided into three sublayers: (i) external porous layer, enriched in P, O, and Zn (Electrolyte 1) and depleted in Ca, Mg, and Cu (Electrolyte 2) and Ti, but also the most contaminated (CO_2, C_2H_5OH); (ii) semiporous layer, enriched in Ca, Mg, P, O, and Zn (Electrolyte 1) or Cu (Electrolyte 2), and depleted in Ti; (iii) transition layer, in which the titanium signal increases and depletion of all other elements (P, O, Ca, Mg, Zn, and Cu) is detected. On the basis of these XPS data, it was possible to conclude that the extreme surface of the coatings most likely consists of titanium (Ti^{4+}), calcium (Ca^{2+}), magnesium (Mg^{2+}), and oxygen with PO_4^{3-}, HPO_4^{2-}, $H_2PO_4^{-}$, and $P_2O_7^{4-}$ as well as Zn^{2+} or Cu^{+}/Cu^{2+}. Furthermore, the XRD analysis suggests that increasing voltage results in amorphization of the coatings, with the detection of crystalline phases such as $Ca(H_2PO_4)_2 \cdot H_2O$ and/or $Ti(HPO_4)_2 \cdot H_2O$.

It was also observed that using zinc ions as a bactericidal element instead of the copper ions in PEO coatings obtained on titanium substrate results in a drastic increase of magnesium incorporated into the obtained structure, combined with a slight increase of calcium ions. The results presented in this paper may be used to design biocompatible and bactericidal coatings due to the creation hydroxyapatite-like structures, in which the Ca^{2+} may be replaced by others, i.e., Mg^{2+}, Zn^{2+}, Cu^{2+}, and the hydroxy group (OH^{-}) by Cu^{+} ions. It should be pointed out that while magnesium accelerates the healing of postoperative wounds, the structure composed of calcium and phosphorus is bone-like. Therefore, zinc or copper added in controlled quantities would perform antibacterial functions, which, together with magnesium, would allow faster healing of postoperative wounds.

5. Conclusions

- It is possible to obtain porous calcium–magnesium–phosphate coatings enriched with copper or zinc.
- The higher the voltage of PEO treatment, the thicker the porous coatings.
- The higher the voltage of PEO treatment, the higher the amount of built-in elements coming from the electrolyte and more amorphous phase in coatings.
- The top 10 nm layer of the studied coatings consist mainly of Ti^{4+}, Ca^{2+}, Mg^{2+} and PO_4^{3-}, HPO_4^{2-}, H_2PO_4.

Author Contributions: K.R. and T.H. conceived and designed the experiments; K.R., S.G., P.C., Ł.D., S.R., D.M., and W.M. performed the experiments; K.R., K.P., and Ł.D. analyzed the data; K.R., K.P., and Ł.D. contributed reagents, materials, and analysis tools; K.R. wrote the paper.

Funding: This work was supported by a grant from OPUS 11 of the National Science Centre, Poland, with registration number 2016/21/B/ST8/01952, titled "Development of models of new porous coatings obtained on titanium by Plasma Electrolytic Oxidation in electrolytes containing phosphoric acid with addition of calcium, magnesium, copper and zinc nitrates".

Conflicts of Interest: The authors declare no conflict of interest.

Nomenclature

PEO	Plasma electrolytic oxidation
MAO	Micro arc oxidation
SEM	Scanning electron microscopy
EDS	Energy dispersive spectroscopy
GDOES	Glow discharge optical emission spectroscopy
XPS	X-ray photoelectron spectroscopy
XRD	X-ray powder diffraction
$\overline{x}$	Mean
σ	Standard deviation
Q_1	First quartile
Q_2	Second quartile (median)
Q_3	Third quartile
M	Metal (here M = Ca + Mg + Zn or M = Ca+ Mg + Cu)
BE	Binding energy
f	Frequency
DC	Direct current
AC	Alternating current
n.u.	no unit

References

1. Sluginov, N. On luminous phenomen, observed in liquids during electrolysis. *Russ. Phys. Chem. Soc.* **1880**, *12*, 193–203.
2. Braun, F. Ueber Lichtemission an einige Electroden in Electrolyten. *Annalen der Physik und Chemie* **1898**, *65*, 361–364. [CrossRef]
3. Dufford, R.T. Luminescence Associated with Electrolysis. *J. Opt. Soc. Am.* **1929**, *18*, 17–28. [CrossRef]
4. McNeill, W.; Gruss, L.L. Anodic Spark Reaction Processes and Articles. U.S. Patent US3293158, 17 September 1963.
5. Yerokhin, A.L.; Nie, X.; Leyland, A.; Matthews, A.; Dowey, S.J. Plasma electrolysis for surface engineering. *Surf. Coat. Technol.* **1999**, *122*, 73–93. [CrossRef]
6. Yerokhin, A.; Parfenov, E.V.; Matthews, A. In situ impedance spectroscopy of the plasma electrolytic oxidation process for deposition of Ca- and P-containing coatings on Ti. *Surf. Coat. Technol.* **2016**, *301*, 54–62. [CrossRef]
7. Aliasghari, S. Plasma Electrolytic Oxidation of Titanium. Ph.D. Thesis, The University of Manchester, Manchester, UK, 2014; p. 223.
8. Hussein, R.O.; Northwood, D.O.; Nie, X. Coating growth behavior during the plasma electrolytic oxidation process. *J. Vac. Sci. Technol. A* **2010**, *28*, 766–773. [CrossRef]
9. Hussein, R.O.; Nie, X.; Northwood, D.O. An investigation of ceramic coating growth mechanisms in plasma electrolytic oxidation (PEO) processing. *Electrochim. Acta* **2013**, *112*, 111–119. [CrossRef]
10. Monfort, F.; Berkani, A.; Matykina, E.; Skeldon, P.; Thompson, G.E.; Habazaki, H.; Shimizu, K. A tracer study of oxide growth during spark anodizing of aluminum. *J. Electrochem. Soc.* **2005**, *152*, C382–C387. [CrossRef]
11. Hussein, R.O.; Nie, X.; Northwood, D.O.; Yerokhin, A.; Matthews, A. Spectroscopic study of electrolytic plasma and discharging behaviour during the plasma electrolytic oxidation (PEO) process. *J. Phys. D Appl. Phys.* **2010**, *43*, 105203–105215. [CrossRef]
12. Dunleavy, C.S.; Golosnoy, I.O.; Curran, J.A.; Clyne, T.W. Characterisation of discharge events during plasma electrolytic oxidation. *Surf. Coat. Technol.* **2009**, *203*, 3410–3419. [CrossRef]
13. Yerokhin, A.L.; Snizhko, L.O.; Gurevina, N.L.; Leyland, A.; Pilkington, A.; Matthews, A. Discharge characterization in plasma electrolytic oxidation of aluminium. *J. Phys. D Appl. Phys.* **2003**, *36*, 2110–2120. [CrossRef]
14. Nominé, A.; Troughton, S.C.; Nominé, A.V.; Henrion, G.; Clyne, T.W. High speed video evidence for localised discharge cascades during plasma electrolytic oxidation. *Surf. Coat. Technol.* **2015**, *269*, 125–130. [CrossRef]
15. Simchen, F.; Sieber, M.; Lampke, T. Electrolyte influence on ignition of plasma electrolytic oxidation processes on light metals. *Surf. Coat. Technol.* **2017**, *315*, 205–213. [CrossRef]
16. Curran, A.; Clyne, T.W. Thermo-physical properties of plasma electrolytic oxide coatings on aluminium. *Surf. Coat. Technol.* **2005**, *199*, 168–179. [CrossRef]
17. Curran, J.A.; Clyne, T.W. Porosity in plasma electrolytic oxide coatings. *Acta Mater.* **2006**, *54*, 1985–1993. [CrossRef]

18. Snizhko, L.O.; Yerokhin, A.L.; Gurevina, N.L.; Patalakha, V.A.; Matthews, A. Excessive oxygen evolution during plasma electrolytic oxidation of aluminium. *Thin Solid Films* **2007**, *516*, 460–464. [CrossRef]
19. Martin, J.; Melhem, A.; Shchedrina, I.; Duchanoy, T.; Nominè, A.; Henrion, G.; Czerwiec, T.; Belmonte, T. Effects of electrical parameters on plasma electrolytic oxidation of aluminium. *Surf. Coat. Technol.* **2013**, *221*, 70–76. [CrossRef]
20. Yerokhin, A.L.; Lyubimov, V.V.; Ashitkov, R.V. Phase formation in ceramic coatings during plasma electrolytic oxidation of aluminium alloys. *Ceram. Int.* **1998**, *24*, 1–6. [CrossRef]
21. Tillous, K.; Toll-Duchanoy, T.; Bauer-Grosse, E.; Hericher, L.; Geandier, G. Microstructure and phase composition of microarc oxidation surface layers formed on aluminium and its alloys 2214-T6 and 7050-T74. *Surf. Coat. Technol.* **2009**, *203*, 2969–2973. [CrossRef]
22. Liu, C.; Liu, P.; Huang, Z.; Yan, Q.; Guo, R.; Li, D.; Jiang, G.; Shen, D. The correlation between the coating structure and the corrosion behavior of the plasma electrolytic oxidation coating on aluminum. *Surf. Coat. Technol.* **2016**, *286*, 223–230. [CrossRef]
23. Hariprasad, S.; Ashfaq, M.; Arunnellaiappan, T.; Harilal, M.; Rameshbabu, N. Role of electrolyte additives on in-vitro corrosion behavior of DC plasma electrolytic oxidization coatings formed on CP-Ti. *Surf. Coat. Technol.* **2016**, *292*, 20–29.
24. Rokosz, K.; Hryniewicz, T.; Kacalak, W.; Tandecka, K.; Raaen, S.; Gaiaschi, S.; Chapon, P.; Malorny, W.; Matýsek, D.; Dudek, Ł.; et al. Characterization of Porous Phosphate Coatings Enriched with Calcium, Magnesium, Zinc and Copper Created on CP Titanium Grade 2 by Plasma Electrolytic Oxidation. *Metals* **2018**, *8*, 411. [CrossRef]
25. Matykina, E.; Arrabal, R.; Skeldon, P.; Thompson, G.E. Investigation of the growth processes of coatings formed by AC plasma electrolytic oxidation of aluminium. *Surf. Coat. Technol.* **2009**, *54*, 6767–6778. [CrossRef]
26. Matykina, E.; Arrabal, R.; Skeldon, P.; Thompson, G.E. Incorporation of zirconia nanoparticles into coatings formed on aluminium by AC plasma electrolytic oxidation. *J. Appl. Electrochem.* **2008**, *38*, 1375–1383. [CrossRef]
27. Dehnavi, V.; Luan, B.L.; Liu, X.Y.; Shoesmith, D.W.; Rohani, S. Correlation between plasma electrolytic oxidation treatment stages and coating microstructure on aluminum under unipolar pulsed DC mode. *Surf. Coat. Technol.* **2015**, *269*, 91–99. [CrossRef]
28. Fatkullin, A.R.; Parfenov, E.V.; Yerokhin, A.; Lazarev, D.M.; Matthews, A. Effect of positive and negative pulse voltages on surface properties and equivalent circuit of the plasma electrolytic oxidation process. *Surf. Coat. Technol.* **2015**, *284*, 427–437. [CrossRef]
29. Krzakala, A.; Kazek-Kesik, A.; Simka, W. Application of plasma electrolytic oxidation to bioactive surface formation on titanium and its alloys. *RSC Adv.* **2013**, *3*, 19725–19743. [CrossRef]
30. Rokosz, K.; Hryniewicz, T.; Raaen, S. Development of Plasma Electrolytic Oxidation for improved Ti6Al4V biomaterial surface properties. *Int. J. Adv. Manuf. Technol.* **2016**, *85*, 2425–2437. [CrossRef]
31. Rokosz, K.; Hryniewicz, T.; Matysek, D.; Raaen, S.; Valíček, J.; Dudek, Ł.; Harničárová, M. SEM, EDS and XPS analysis of the coatings obtained on titanium after plasma electrolytic oxidation in electrolytes containing copper nitrate. *Materials* **2016**, *9*, 318. [CrossRef] [PubMed]
32. Rokosz, K.; Hryniewicz, T.; Raaen, S.; Chapon, P. Development of copper-enriched porous coatings on ternary Ti-Nb-Zr alloy by Plasma Electrolytic Oxidation. *Int. J. Adv. Manuf. Technol.* **2017**, *89*, 2953–2965. [CrossRef]
33. Wang, S.; Zhao, Q.; Liu, D.; Du, N. Microstructure and elevated temperature tribological behavior of TiO_2/Al_2O_3 composite ceramic coating formed by microarc oxidation of Ti6Al4V alloy. *Surf. Coat. Technol.* **2015**, *272*, 343–349. [CrossRef]
34. Ma, C.; Zhang, M.; Yuan, Y.; Jing, X.; Bai, X. Tribological behavior of plasma electrolytic oxidation coatings on the surface of Mg–8Li–1Al alloy. *Tribol. Int.* **2012**, *47*, 62–68. [CrossRef]
35. Rokosz, K.; Hryniewicz, T.; Gaiaschi, S.; Chapon, P.; Raaen, S.; Pietrzak, S.; Malorny, W.; Fernandes, J.S. Characterization of Porous Phosphate Coatings Enriched with Magnesium or Zinc on CP Titanium Grade 2 under DC Plasma Electrolytic Oxidation. *Metals* **2018**, *8*, 112. [CrossRef]
36. Sowa, M.; Simka, W. Effect of DC Plasma Electrolytic Oxidation on Surface Characteristics and Corrosion Resistance of Zirconium. *Materials* **2018**, *11*, 723. [CrossRef] [PubMed]

37. Liu, C.; He, D.; Yan, Q.; Huang, Z.; Liu, P.; Li, D.; Jiang, G.; Ma, H.; Nash, P.; Shen, D. An investigation of the coating/substrate interface of plasma electrolytic oxidation coated aluminum. *Surf. Coat. Technol.* **2015**, *280*, 86–91. [CrossRef]
38. Gu, W.; Lv, G.; Chen, H.; Chen, G.; Feng, W.; Yang, S. Characterisation of ceramic coatings produced by plasma electrolytic oxidation of aluminum alloy. *Mater. Sci. Eng. A* **2007**, *447*, 158–162. [CrossRef]
39. Zhu, L.; Guo, Z.; Zhang, Y.; Li, Z.; Sui, M. A mechanism for the growth of a plasma electrolytic oxide coating on Al. *Electrochim. Acta* **2016**, *208*, 296–303. [CrossRef]
40. Tillous, E.K.; Toll-Duchanoy, T.; Bauer-Grosse, E. Microstructure and 3D microtomographic characterization of porosity of MAO surface layers formed on aluminium and 2214-T6 alloy. *Surf. Coat. Technol.* **2009**, *203*, 1850–1855. [CrossRef]
41. Li, Q.; Liu, C.; Yang, W.; Liang, J. Growth mechanism and adhesion of PEO coatings on 2024 Al alloy. *Surf. Eng.* **2017**, *33*, 760–766. [CrossRef]
42. Wang, Z.; Wu, L.; Qi, Y.; Cai, W.; Jiang, Z. Self-lubricating Al_2O_3/PTFE composite coating formation on surface of aluminium alloy. *Surf. Coat. Technol.* **2010**, *204*, 3315–3318. [CrossRef]
43. Li, W.; Qian, Z.; Liu, X.; Zhu, L.; Liu, H. Investigation of micro-arc oxidation coating growth patterns of aluminum alloy by two-step oxidation method. *Appl. Surf. Sci.* **2015**, *356*, 581–586. [CrossRef]
44. Zhang, X.M.; Chen, D.F.; Gong, X.Z.; Yang, S.Q.; Tian, X.B. Modulation effects of K_2ZrF_6 additive on microstructure and heat resistance of micro-arc oxide coatings fabricated on LY12 aluminum alloy. *J. Inorg. Mater.* **2010**, *25*, 865–870. [CrossRef]
45. Yang, J.; Lu, X.; Blawert, C.; Di, S.; Zheludkevich, M.L. Microstructure and corrosion behavior of Ca/P coatings prepared on magnesium by plasma electrolytic oxidation. *Surf. Coat. Technol.* **2017**, *319*, 359–369. [CrossRef]
46. Lu, X.; Blawert, C.; Huang, Y.; Ovri, H.; Zheludkevich, M.L.; Kainer, K.U. Plasma electrolytic oxidation coatings on Mg alloy with addition of SiO_2 particles. *Electrochim. Acta* **2016**, *187*, 20–33. [CrossRef]
47. Lu, X.; Blawert, C.; Kainer, K.U.; Zheludkevich, M.L. Investigation of the formation mechanisms of plasma electrolytic oxidation coatings on Mg alloy AM50 using particles. *Electrochim. Acta* **2016**, *196*, 680–691. [CrossRef]
48. Ma, H.; Li, D.; Liu, C.; Huang, Z.; He, D.; Yan, Q.; Liu, P.; Nash, P.; Shen, D.J. An investigation of $(NaPO_3)_6$ effects and mechanisms during micro-arc oxidation of AZ31 magnesium alloy. *Surf. Coat. Technol.* **2015**, *266*, 151–159. [CrossRef]
49. Ezhilselvi, V.; Nithin, J.; Balaraju, J.N.; Subramanian, S. The influence of current density on the morphology and corrosion properties of MAO coatings on AZ31B magnesium alloy. *Surf. Coat. Technol.* **2016**, *288*, 221–229. [CrossRef]
50. Sobrinho, P.H.; Savguira, Y.; Ni, Q.; Thorpe, S.J. Statistical analysis of the voltage-time response produced during PEO coating of AZ31B magnesium alloy. *Surf. Coat. Technol.* **2017**, *315*, 530–545. [CrossRef]
51. Lu, X.; Sah, S.P.; Scharnagl, N.; Störmer, M.; Starykevich, M.; Mohedano, M.; Blawert, C.; Zheludkevich, M.L.; Kainer, K.U. Degradation behavior of PEO coating on AM50 magnesium alloy produced from electrolytes with clay particle addition. *Surf. Coat. Technol.* **2015**, *269*, 155–169. [CrossRef]
52. Pezzato, L.; Brunelli, K.; Gross, S.; Magrini, M.; Dabalà, M. Effect of process parameters of plasma electrolytic oxidation on microstructure and corrosion properties of magnesium alloys. *J. Appl. Electrochem.* **2014**, *44*, 867–879. [CrossRef]
53. Zhang, R.F.; Zhang, S.F.; Xiang, J.H.; Zhang, L.H.; Zhang, Y.Q.; Guo, S.B. Influence of sodium silicate concentration on properties of micro arc oxidation coatings formed on AZ91HP magnesium alloys. *Surf. Coat. Technol.* **2012**, *206*, 5072–5079. [CrossRef]
54. Cao, F.H.; Lin, L.Y.; Zhang, Z.; Zhang, J.Q.; Cao, C.N. Environmental friendly plasma electrolytic oxidation of AM60 magnesium alloy and its corrosion resistance. *Trans. Nonferrous Met. Soc. China* **2008**, *18*, 240–247. [CrossRef]
55. Tang, H.; Xin, T.Z.; Sun, Q.; Yi, C.G.; Jiang, Z.H.; Wang, F.P. Influence of $FeSO_4$ concentration on thermal emissivity of coatings formed on titanium alloy by micro-arc oxidation. *Appl. Surf. Sci.* **2011**, *257*, 10839–10844. [CrossRef]
56. Shokouhfar, M.; Allahkaram, S.R. Formation mechanism and surface characterization of ceramic composite coatings on pure titanium prepared by micro-arc oxidation in electrolytes containing nanoparticles. *Surf. Coat. Technol.* **2016**, *291*, 396–405. [CrossRef]

57. Rokosz, K.; Hryniewicz, T.; Dudek, Ł.; Matysek, D.; Valíček, J.; Harničárová, M. SEM and EDS analysis of surface layer formed on titanium after plasma electrolytic oxidation in H_3PO_4 with the addition of $Cu(NO_3)_2$. *J. Nanosci. Nanotechnol.* **2016**, *16*, 7814–7817. [CrossRef]
58. Liu, S.M.; Yang, X.J.; Cui, Z.D.; Zhu, S.L.; Wei, Q. One-step synthesis of petal-like apatite/titania composite coating on a titanium by micro-arc treating. *Mater. Lett.* **2011**, *65*, 1041–1044. [CrossRef]
59. Yan, Y.Y.; Sun, J.F.; Han, Y.; Li, D.C.; Cui, K. Microstructure and bioactivity of Ca, P and Sr doped TiO_2 coating formed on porous titanium by micro-arc oxidation. *Surf. Coat. Technol.* **2010**, *205*, 1702–1713. [CrossRef]
60. Rokosz, K.; Hryniewicz, T.; Gaiaschi, S.; Chapon, P.; Raaen, S.; Pietrzak, K.; Malorny, W. Characterisation of calcium- and phosphorus-enriched porous coatings on CP Titanium Grade 2 fabricated by plasma electrolytic oxidation. *Metals* **2017**, *7*, 354. [CrossRef]
61. Tang, H.; Sun, Q.; Xin, T.Z.; Yi, C.G.; Jiang, Z.H.; Wang, F.P. Influence of $Co(CH_3COO)_2$ concentration on thermal emissivity of coatings formed on titanium alloy by micro-arc oxidation. *Curr. Appl. Phys.* **2012**, *12*, 284–290. [CrossRef]
62. Rudnev, V.S.; Yarovaya, T.P.; Egorkin, V.S.; Sinebryukov, S.L.; Gnedenkov, S.V. Properties of coatings formed on titanium by plasma electrolytic oxidation in a phosphate-borate electrolyte. *Russ. J. Appl. Chem.* **2010**, *83*, 664–670. [CrossRef]
63. Xu, Y.J.; Yao, Z.P.; Jia, F.Z.; Wang, Y.L.; Jiang, Z.H.; Bu, H.T. Preparation of PEO ceramic coating on Ti alloy and its high temperature oxidation resistance. *Curr. Appl. Phys.* **2010**, *10*, 698–702. [CrossRef]
64. Qiao, L.P.; Lou, J.; Zhang, S.F.; Qu, B.; Chang, W.H.; Zhang, R.F. The entrance mechanism of calcium and phosphorus elements into micro arc oxidation coatings developed on Ti6Al4V alloy. *Surf. Coat. Technol.* **2016**, *285*, 187–196. [CrossRef]
65. Wang, Y.H.; Liu, Z.G.; Ouyang, J.H.; Wang, Y.M.; Zhou, Y. Influence of electrolyte compositions on structure and high-temperature oxidation resistance of microarc oxidation coatings formed on Ti2AlNb alloy. *J. Alloys Compd.* **2015**, *647*, 431–437. [CrossRef]
66. Karbowniczek, J.; Muhaffel, F.; Cempura, G.; Cimenoglu, H.; Filemonowicz, A.C. Influence of electrolyte composition on microstructure, adhesion and bioactivity of micro-arc oxidation coatings produced on biomedical Ti6Al7Nb alloy. *Surf. Coat. Technol.* **2017**, *321*, 97–107. [CrossRef]
67. Montazeri, M.; Dehghanian, C.; Shokouhfar, M.; Baradaran, A. Investigation of the voltage and time effects on the formation of hydroxyapatite-containing titania prepared by plasma electrolytic oxidation on Ti-6Al-4V alloy and its corrosion behavior. *Appl. Surf. Sci.* **2011**, *257*, 7268–7275. [CrossRef]
68. Simka, W.; Sowa, M.; Socha, R.P.; Maciej, A.; Michalska, J. Anodic oxidation of zirconium in silicate solutions. *Electrochim. Acta* **2013**, *104*, 518–525. [CrossRef]
69. Sowa, M.; Dercz, G.; Suchanek, K.; Simka, W. Investigation of anodic oxide coatings on zirconium after heat treatment. *Appl. Surf. Sci.* **2015**, *346*, 534–542. [CrossRef]
70. Matykina, E.; Arrabal, R.; Skeldon, P.; Thompson, G.E.E.; Wang, P.; Wood, P. Plasma electrolytic oxidation of a zirconium alloy under AC conditions. *Surf. Coat. Technol.* **2010**, *204*, 2142–2151. [CrossRef]
71. Cengiz, S.; Uzunoglu, A.; Stanciu, L.; Tarakci, M.; Gencer, Y. Direct fabrication of crystalline hydroxyapatite coating on zirconium by single-step plasma electrolytic oxidation process. *Surf. Coat. Technol.* **2016**, *301*, 74–79. [CrossRef]
72. Fidan, S.; Muhaffel, F.; Riool, M.; Cempura, G.; de Boer, L.; Zaat, S.A.J.; Filemonowicz, A.C.; Cimenoglu, H. Fabrication of oxide layer on zirconium by micro-arc oxidation: Structural and antimicrobial characteristics. *Mater. Sci. Eng. C* **2017**, *71*, 565–569. [CrossRef] [PubMed]
73. Cengiz, S.; Gencer, Y. The characterization of the oxide based coating synthesized on pure zirconium by plasma electrolytic oxidation. *Surf. Coat. Technol.* **2014**, *242*, 132–140. [CrossRef]
74. Cengiz, S.; Azakli, Y.; Tarakci, M.; Stanciu, L.; Gencer, Y. Microarc oxidation discharge types and bio properties of the coating synthesized on zirconium. *Mater. Sci. Eng. C* **2017**, *77*, 374–383. [CrossRef] [PubMed]
75. Ha, J.-Y.Y.; Tsutsumi, Y.; Doi, H.; Nomura, N.; Kim, K.-H.H.; Hanawa, T. Enhancement of calcium phosphate formation on zirconium by micro-arc oxidation and chemical treatments. *Surf. Coat. Technol.* **2011**, *205*, 4948–4955. [CrossRef]
76. Sandhyarani, M.; Rameshbabu, N.; Venkateswarlu, K.; Rama Krishna, L. Fabrication, characterization and in-vitro evaluation of nanostructured zirconia/hydroxyapatite composite film on zirconium. *Surf. Coat. Technol.* **2014**, *238*, 58–67.

77. Sandhyarani, M.; Prasadrao, T.; Rameshbabu, N. Role of electrolyte composition on structural, morphological and in-vitro biological properties of plasma electrolytic oxidation films formed on zirconium. *Appl. Surf. Sci.* **2014**, *317*, 198–209.
78. Apelfeld, A.V.; Betsofen, S.Y.; Borisov, A.M.; Vladimirov, B.V.; Savushkina, S.V.; Knyazev, E.V. Stabilization of the high-temperature phases in ceramic coatings on zirconium alloy produced by plasma electrolytic oxidation. *J. Phys. Conf. Ser.* **2016**, *748*, 12019. [CrossRef]
79. Apelfeld, A.V.; Ashmarin, A.A.; Borisov, A.M.; Vinogradov, A.V.; Savushkina, S.V.; Shmytkova, E.A. Formation of zirconia tetragonal phase by plasma electrolytic oxidation of zirconium alloy in electrolyte comprising additives of yttria nanopowder. *Surf. Coat. Technol.* **2017**, *328*, 513–517. [CrossRef]
80. Sowa, M.; Simka, W. Electrochemical Impedance and Polarization Corrosion Studies of Tantalum Surface Modified by DC Plasma Electrolytic Oxidation. *Materials* **2018**, *11*, 545. [CrossRef] [PubMed]
81. Sowa, M.; Woszczak, M.; Kazek-Kęsik, A.; Dercz, G.; Korotin, D.M.; Zhidkov, I.S.; Kurmaev, E.Z.; Cholakh, S.O.; Basiaga, M.; Simka, W. Influence of process parameters on plasma electrolytic surface treatment of tantalum for biomedical applications. *Appl. Surf. Sci.* **2017**, *407*, 52–63. [CrossRef]
82. Rokosz, K.; Hryniewicz, T.; Chapon, P.; Raaen, S.; Ricardo Zschommler Sandim, H. XPS and GDOES characterization of porous coating enriched with copper and calcium obtained on tantalum via plasma electrolytic oxidation. *J. Spectrosc.* **2016**, *2016*, 7093071. [CrossRef]
83. Fattah-alhosseini, A.; Pourmahmoud, M. Passive and semiconducting properties assessment of commercially pure tantalum in Hank's physiological solution. *J. Mater. Eng. Perform.* **2018**, *27*, 116–123. [CrossRef]
84. Sowa, M.; Worek, J.; Dercz, G.; Korotin, D.M.; Kukharenko, A.I.; Kurmaev, E.Z.; Cholakh, S.O.; Basiaga, M.; Simka, W. Surface characterisation and corrosion behaviour of niobium treated in a Ca- and P-containing solution under sparking conditions. *Electrochim. Acta* **2016**, *198*, 91–103. [CrossRef]
85. Sowa, M.; Simka, W. Electrochemical behavior of plasma electrolytically oxidized niobium in simulated physiological environment. *Surf. Coat. Technol.* **2018**, *344*, 21–131. [CrossRef]
86. Rokosz, K.; Hryniewicz, T. Comparative SEM and EDX analysis of surface coatings created on niobium and titanium alloys after Plasma Electrolytic Oxidation (PEO). *Tehnički Vjesnik-Technical Gazette* **2017**, *24*, 465–472.
87. Gomes, M.A.B.; Onofre, S.; Juanto, S.; Bulhões, L.O.S. Anodization of niobium in sulphuric acid media. *J. Appl. Electrochem.* **1991**, *21*, 1023–1026. [CrossRef]
88. Pereira, B.L.; Lepienski, C.M.; Mazzaro, I.; Kuromoto, N.K. Apatite grown in niobium by two-step plasma electrolytic oxidation. *Mater. Sci. Eng. C Mater.* **2017**, *77*, 1235–1241. [CrossRef] [PubMed]
89. Stojadinović, S.; Tadić, N.; Vasilic, R. Plasma electrolytic oxidation of hafnium. *J. Refract. Met. Hard Mater.* **2017**, *69*, 153–157. [CrossRef]
90. Han, Y.; Hong, S.H.; Xu, K.W. Synthesis of nanocrystalline titania films by micro-arc oxidation. *Mater. Lett.* **2002**, *56*, 744–747. [CrossRef]
91. Han, Y.; Xu, K. Photoexcited formation of bone apatite-like coatings on micro-arc oxidized titanium. *J. Biomed. Mater. Res.* **2004**, *71A*, 608–614. [CrossRef] [PubMed]
92. Huang, P.; Xu, K.W.; Han, Y. Preparation and apatite layer formation of plasma electrolytic oxidation film on titanium for biomedical application. *Mater. Lett.* **2005**, *59*, 185–189. [CrossRef]
93. Song, W.H.; Jun, Y.K.; Han, Y.; Hong, S.H.; Kim, H.E.; Heo, S.J.; Koak, J.Y. Biomimetic apatite coatings on micro-arc oxidized titania. *Biomaterials* **2004**, *25*, 3341–3349. [CrossRef] [PubMed]
94. Zhang, Y.M.; Bataillon-Linez, P.; Huang, P.; Zhao, Y.M.; Han, Y.; Traisnel, M.; Xu, K.W.; Hildebrand, H.F. Surface analyses of micro-arc oxidized and hydrothermally treated titanium and effect on osteoblast behavior. *J. Biomed. Mater. Res.* **2003**, *68*, 383–391. [CrossRef] [PubMed]
95. Li, L.H.; Kong, Y.M.; Kim, H.W.; Kim, Y.W.; Kim, H.E.; Heo, S.J.; Koak, J.Y. Improved biological performance of Ti implants due to surface modification by micro-arc oxidation. *Biomaterials* **2004**, *25*, 2867–2875. [CrossRef] [PubMed]
96. Lee, S.H.; Kim, H.W.; Lee, E.J.; Li, L.H.; Kim, H.E. Hydroxyapatite–TiO_2 hybrid coating on Ti implants. *J. Biomater. Appl.* **2006**, *20*, 194–208. [CrossRef] [PubMed]
97. Han, Y.; Hong, S.H.; Xu, K.W. Structure and in vitro bioactivity of titania-based films by micro-arc oxidation. *Surf. Coat. Technol.* **2003**, *168*, 249–258. [CrossRef]
98. Teh, T.H.; Berkani, A.; Mato, S.; Skeldon, P.; Thompson, G.E.; Habazaki, H.; Shimizu, K. Initial stages of plasma electrolytic oxidation of titanium. *Corros. Sci.* **2003**, *45*, 2757–2768. [CrossRef]

99. Rudnev, V.S.; Vasilyeva, M.S.; Kondrikov, N.B.; Tyrina, L.M. Plasma-electrolytic formation, composition and catalytic activity of manganese oxide containing structures on titanium. *Appl. Surf. Sci.* **2005**, *252*, 1211–1220. [CrossRef]
100. Ryu, H.S.; Song, W.H.; Hong, S.H. Biomimetic apatite induction on Ca-containing titania. *Curr. Appl. Phys.* **2005**, *5*, 512–515. [CrossRef]
101. Chen, J.Z.; Shi, Y.L.; Wang, L.; Yan, F.Y.; Zhang, F.Y. Preparation and properties of hydroxyapatite-containing titania coating by micro-arc oxidation. *Mater. Lett.* **2006**, *60*, 2538–2543. [CrossRef]
102. Matykina, E.; Montuori, M.; Gough, J.; Monfort, F.; Berkani, A.; Skeldon, P.; Thompson, G.E.; Habazaki, H. Spark anodising of titanium for biomedical applications. *Trans. IMF* **2006**, *84*, 125–133. [CrossRef]
103. Han, I.H.; Choi, J.H.; Zhao, B.H.; Baik, H.K.; Lee, I.S. Effects of electrical wave form on pore size of micro-arc oxidized TiO_2 film. *Key Eng. Mater.* **2006**, *309–311*, 375–378. [CrossRef]
104. Shokouhfar, M.; Dehghanian, C.; Montazeri, M.; Baradaran, A. Preparation of ceramic coating on Ti substrate by plasma electrolytic oxidation in different electrolytes and evaluation of its corrosion resistance: Part II. *Appl. Surf. Sci.* **2012**, *258*, 2416–2423. [CrossRef]
105. Zhu, L.; Ye, X.; Tang, G.; Zhao, N.; Gong, Y.; Zhao, Y.; Zhao, J.; Zhang, X. Corrosion test, cell behavior test, and in vivo study of gradient TiO_2 layers produced by compound electrochemical oxidation. *J. Biomed. Mater. Res. A* **2006**, *78*, 515–522. [CrossRef] [PubMed]
106. Habazaki, H.; Onodera, T.; Fushimi, K.; Konno, H.; Toyotake, K. Spark anodizing of β-Ti alloy for wear-resistant coating. *Surf. Coat. Technol.* **2007**, *201*, 8730–8737. [CrossRef]
107. Kim, M.S.; Ryu, J.J.; Sung, Y.M. One-step approach for nano-crystalline hydroxyapatite coating on titanium via micro-arc oxidation. *Electrochem. Commun.* **2007**, *9*, 1886–1891. [CrossRef]
108. Ragalevičius, R.; Stalnionis, G.; Niaura, G.; Jagminas, A. Micro-arc oxidation of Ti in a solution of sulfuric acid and Ti^{+3} salt. *Appl. Surf. Sci.* **2008**, *254*, 1608–1613. [CrossRef]
109. Zhang, W.; Du, K.; Yan, C.; Wang, F. Preparation and characterization of a novel Si-incorporated ceramic film on pure titanium by plasma electrolytic oxidation. *Appl. Surf. Sci.* **2008**, *254*, 5216–5223. [CrossRef]
110. Lebukhova, N.V.; Rudnev, V.S.; Kirichenko, E.A.; Chigrin, P.G.; Lukiyanchuk, I.V.; Yarovaya, T.P. Effect of the structure of the oxidized titanium surface on the particle size and properties of the deposited copper-molybdate catalyst. *Prot. Met. Phys. Chem. Surf.* **2016**, *52*, 1024–1030. [CrossRef]
111. Terleeva, O.P.; Sharkeev, Y.P.; Slonova, A.I.; Mironov, I.V.; Legostaeva, E.V.; Khlusov, I.A.; Matykina, E.; Skeldon, P.; Thompson, G.E. Effect of microplasma modes and electrolyte composition on micro-arc oxidation coatings on titanium for medical applications. *Surf. Coat. Technol.* **2010**, *205*, 1723–1729. [CrossRef]
112. Wang, Y.M.; Lei, T.Q.; Jiang, B.L.; Guo, L.X. Growth, microstructure and mechanical properties of microarc oxidation coatings on titanium alloy in phosphate-containing solution. *Appl. Surf. Sci.* **2004**, *233*, 258–267. [CrossRef]
113. Tang, H.; Sun, Q.; Yi, C.G.; Jiang, Z.H.; Wang, F.P. High emissivity coatings on titanium alloy prepared by micro-arc oxidation for high temperature application. *J. Mater. Sci.* **2012**, *47*, 2162–2168. [CrossRef]
114. Santos, A.D.; Araujo, J.R.; Landi, S.M.; Kuznetsov, A.; Granjeiro, J.M.; Sena, L.A.D.; Achete, C.A. A study of the physical, chemical and biological properties of TiO_2 coatings produced by micro-arc oxidation in a Ca-P-based electrolyte. *J. Mater. Sci. Mater. Med.* **2014**, *25*, 1769–1780. [CrossRef] [PubMed]
115. Li, Q.B.; Yang, W.B.; Liu, C.C.; Wang, D.A.; Liang, J. Correlations between the growth mechanism and properties of micro-arc oxidation coatings on titanium alloy: Effects of electrolytes. *Surf. Coat. Technol.* **2017**, *316*, 162–170. [CrossRef]
116. Sharifi, H.; Aliofkhazraei, M.; Darband, G.; Rouhaghdam, A.S. Characterization of PEO nanocomposite coatings on titanium formed in electrolyte containing atenolol. *Surf. Coat. Technol.* **2016**, *304*, 438–449. [CrossRef]
117. Zhu, X.L.; Chen, J.; Scheideler, L.; Reichl, R.; Geis-Gerstorfer, J. Effects of topography and composition of titanium surface oxides on osteoblast responses. *Biomaterials* **2004**, *25*, 4087–4103. [CrossRef] [PubMed]
118. Geetha, M.; Singh, A.K.; Asokamani, R.; Gogia, A.K. Ti based biomaterials, the ultimate choice for orthopaedic implants—A review. *Prog. Mater. Sci.* **2009**, *54*, 397–425. [CrossRef]
119. Jayaraman, M.; Meyer, U.; Bühner, M.; Joos, U.; Wiesmann, H.P. Influence of titanium surfaces on attachment of osteoblast-like cells in vitro. *Biomaterials* **2004**, *25*, 625–631. [CrossRef]

120. Cai, Y.L.; Zhang, J.J.; Zhang, S.; Venkatraman, S.S.; Zeng, X.T.; Du, H.J.; Mondal, D. Osteoblastic cell response on fluoridated hydroxyapatite coatings: The effect of magnesium incorporation. *Biomed. Mater.* **2010**, *5*, 054114. [CrossRef] [PubMed]
121. Piocha, D.; Zima, A.; Paszkiewicz, Z.; Slosarczyk, A. Physicochemical properties of the novel biphasic hydroxyapatite–magnesium phosphate biomaterial. *Acta Bioeng. Biomech.* **2013**, *15*, 53–63.
122. Grigolato, R.; Pizzi, N.; Brotto, M.C.; Corrocher, G.; Desando, G.; Grigolo, B. Magnesium-enriched hydroxyapatite as bone filler in an ameloblastoma mandibular defect. *Int. J. Clin. Exp. Med.* **2015**, *8*, 281–288. [PubMed]
123. Nygren, H.; Bigdeli, N.; Ilver, L.; Malmberg, P. Mg-corrosion, hydroxyapatite, and bone healing. *Biointerphases* **2017**, *12*, 02C407. [CrossRef] [PubMed]
124. Laurencin, D.; Almora-Barrios, N.; de Leeuw, N.H.; Gervais, C.; Bonhomme, C.; Mauri, F.; Chrzanowski, W.; Knowles, J.C.; Newport, R.J.; Wong, A.; et al. Magnesium incorporation into hydroxyapatite. *Biomaterials* **2011**, *32*, 1826–1837. [CrossRef] [PubMed]
125. Farzadi, A.; Bakhshi, F.; Solati-Hashjin, M.; Asadi-Eydivand, M.; Abu Osman, A.A. Magnesium incorporated hydroxyapatite: Synthesis and structural properties characterization. *Ceram. Int.* **2014**, *40*, 6021–6029. [CrossRef]
126. Hu, H.; Zhang, W.; Qiao, Y.; Jiang, X.; Liu, X.; Ding, C. Antibacterial activity and increased bone marrow stem cell functions of Zn-incorporated TiO_2 coatings on titanium. *Acta Biomater.* **2012**, *8*, 904–915. [CrossRef] [PubMed]
127. Zhang, X.; Wang, H.; Li, J.; He, X.; Hang, R.; Huang, X.; Tian, L.; Tang, B. Corrosion behavior of Zn-incorporated antibacterial TiO_2 porous coating on titanium. *Ceram. Int.* **2016**, *42*, 17095–17100. [CrossRef]
128. Zhang, L.; Gao, Q.; Han, Y. Zn and Ag co-doped anti-microbial TiO_2 coatings on Ti by micro-arc oxidation. *J. Mater. Sci. Technol.* **2016**, *32*, 919–924. [CrossRef]
129. Zhang, J.Y.; Ai, H.J.; Qi, M. Osteoblast growth on the surface of porous Zn-containing HA/TiO_2 hybrid coatings on Ti substrate by MAO plus sol-gel methods. *Surf. Coat. Technol.* **2013**, *228*, S202–S205. [CrossRef]
130. Zhao, B.H.; Zhang, W.; Wang, D.N.; Feng, W.; Liu, Y.; Lin, Z.; Du, K.Q.; Deng, C.F. Effect of Zn content on cytoactivity and bacteriostasis of micro-arc oxidation coatings on pure titanium. *Surf. Coat. Technol.* **2013**, *228*, S428–S432. [CrossRef]
131. Jin, G.D.; Qin, H.; Cao, H.L.; Qian, S.; Zhao, Y.C.; Peng, X.C.; Zhang, X.L.; Liu, X.Y.; Chu, P.K. Synergistic effects of dual Zn/Ag ion implantation in osteogenic activity and antibacterial ability of titanium. *Biomaterials* **2014**, *35*, 7699–7713. [CrossRef] [PubMed]
132. Huang, Y.; Zhang, X.J.; Mao, H.H.; Li, T.T.; Zhao, R.L.; Yan, Y.J.; Pang, X.F. Osteoblastic cell responses and antibacterial efficacy of Cu/Zn co-substitued hydroxyapatite coatings on pure titanium using electrodeposition method. *RSC Adv.* **2015**, *5*, 17076–17086. [CrossRef]
133. Rokosz, K.; Hryniewicz, T.; Gaiaschi, S.; Chapon, P.; Raaen, S.; Malorny, W.; Matysek, W.; Pietrzak, K. Development of porous coatings enriched with magnesium and zinc obtained by DC Plasma Electrolytic Oxidation. *Micromachines* **2018**, *9*, 332. [CrossRef]
134. Zhao, L.Z.; Chu, P.K.; Zhang, Y.M.; Wu, Z.F. Antibacterial coatings on titanium implants. *J. Biomed. Mater. Res. Part B* **2009**, *91*, 470–480. [CrossRef] [PubMed]
135. Zhu, W.; Zhang, Z.; Gu, B.; Sun, J.; Zhu, L. Biological activity and antibacterial property of nano-structured TiO_2 coating incorporated with Cu prepared by micro-arc oxidation. *J. Mater. Sci. Technol.* **2013**, *29*, 237–244. [CrossRef]
136. Zhang, L.; Guo, J.; Huang, X.; Zhang, Y.; Han, Y. The dual function of Cu-doped TiO_2 coatings on titanium for application in percutaneous implants. *J. Mater. Chem. B* **2016**, *4*, 3788–3800. [CrossRef]
137. Moulder, J.F.; Stickle, W.F.; Sobol, P.E.; Bomben, K.D. *Handbook of X-ray Photoelectron Spectroscopy*; Perkin-Elmer Corporation: Eden Prairie, MN, USA, 1992.
138. Wagner, C.D.; Naumkin, A.V.; Kraut-Vass, A.; Allison, J.W.; Powell, C.J.; Rumble, J.R., Jr. NIST Standard Reference Database 20, Version 3.4. 2003. Available online: http://srdata.nist.gov/xps (accessed on 1 July 2018).
139. Casa Software Ltd. CasaXPS: Processing Software for XPS, AES, SIMS and More. 2009. Available online: http://www.casaxps.com (accessed on 1 July 2018).

140. Gaiaschi, S.; Richard, S.; Chapon, P.; Acher, O. Real-time measurement in glow discharge optical emission spectrometry via differential interferometric profiling. *J. Anal. Atom. Spectrom.* **2017**, *32*, 1798–1804. [CrossRef]
141. Pulsed RF Glow Discharge Optical Emission Spectrometry—Ultra Fast Elemental Depth Profiling, HORIBA Scientific, Printed in France—©HORIBA Jobin Yvon. 2014, p. 7. Available online: http://www.horiba.com/scientific/products/atomic-emission-spectroscopy/glow-discharge/ (accessed on 1 July 2018).